

A Generic and Efficient E-field Parallel Imaging Correlator for Next-Generation Radio Telescopes

Nithyanandan Thyagarajan,^{1*} Adam P. Beardsley,¹ Judd D. Bowman¹
and Miguel F. Morales²

¹*Arizona State University, School of Earth and Space Exploration, Tempe, AZ 85287, USA*

²*University of Washington, Department of Physics, Seattle, WA 98195, USA*

Accepted XXX. Received YYY; in original form ZZZ

ABSTRACT

Modern radio telescopes are favouring densely packed array layouts with large numbers of antennas ($N_A \gtrsim 1000$). Since the complexity of traditional correlators scales as $\mathcal{O}(N_A^2)$, there will be a steep cost for realizing the full imaging potential of these powerful instruments. Through our generic and efficient E-field Parallel Imaging Correlator (EPIC), we present the first software demonstration of a generalized direct imaging algorithm, namely, the Modular Optimal Frequency Fourier (MOFF) imager. It takes advantage of the multiplication-convolution theorem of Fourier transforms. Not only does it bring down the cost for dense layouts to $\mathcal{O}(N_A \log_2 N_A)$ but can also image from irregular layouts and heterogeneous arrays of antennas. We demonstrate its versatility to image with heterogeneous arrays by showing that it robustly estimates the input sky model while wrong assumptions about array homogeneity lead to severe mis-estimates. EPIC is highly modular and parallelizable, implemented in object oriented Python, and publicly available. We have verified the images produced to be equivalent to those produced using traditional techniques to within a precision set by gridding coarseness. We have also validated our implementation on data observed with the Long Wavelength Array (LWA). Antenna layouts with dense filling factors consisting of a large number of antennas such as LWA, the Square Kilometre Array, Hydrogen Epoch of Reionization Array, and Canadian Hydrogen Intensity Mapping Experiment will gain significant computational advantage by deploying EPIC. Inherent availability of calibrated time-domain images on digitizer writeout time-scales and vastly lower I/O bandwidth relative to visibility-based systems will make it a prime candidate for transient searches of Fast Radio Bursts (FRB) as well as planetary and exoplanetary phenomena.

Key words: instrumentation: interferometers – techniques: image processing – techniques: interferometric

1 INTRODUCTION

Radio astronomy is entering an era in which interferometers of hundreds to thousands of individual antennas are needed to achieve desired survey speeds. Nowhere is this more apparent than at radio frequencies below 1.4 GHz. The study of the history of hydrogen gas throughout the universe’s evolution is pushing technology development towards arrays of low-cost antennas with large fields of view and densely packed layouts. Similarly, the search for transient objects and regular monitoring of the time-dependent sky is driving

instruments in the same direction with the added requirement of fast read-outs. A number of new telescopes are being or were developed around the world based on this new paradigm, including the Hydrogen Epoch of Reionization Array¹ (HERA; DeBoer et al. 2016), the Murchison Wide-field Array (MWA; Tingay et al. 2013; Bowman et al. 2013), the Precision Array for Probing the Epoch of Reionization (PAPER; Parsons et al. 2010), the LOw Frequency ARray (LOFAR; van Haarlem et al. 2013), the Canadian Hydrogen Intensity Mapping Experiment (CHIME; Bandura et al. 2014), the Long Wavelength Array (LWA; Ellingrod et al.

* E-mail: t_nithyanandan@asu.edu

¹ <http://reionization.org>

2013), and the low frequency Square Kilometer Array (SKA1-Low; Mellema et al. 2013).

This paradigm shift requires a fundamentally new approach to the design of digital correlators (Lonsdale et al. 2000). Modern correlators calculate the cross-power correlation between all antenna pairs in many narrow frequencies, forming *visibilities*, the fundamental measurement of traditional radio interferometers. The computational requirements for a modern FX correlator scale with the number of antenna pairs, or the square of the number of antennas $\sim N_A^2$ (Bunton 2004). For this reason traditional correlators have difficulty scaling to thousands of antennas. As an example, the full HERA correlator for 352 dishes with 200 MHz of bandwidth requires 212 trillion complex multiplies and adds per second (TMACS). Future arrays with thousands of collecting elements will require orders of magnitude more computation, making the correlator the dominant cost.

For certain classes of radio arrays there is an alternative to the FX correlator that can lower the computational burden by directly performing a spatial Fast Fourier Transform (FFT; Cooley & Tukey 1965) on the electric fields measured by each antenna in the array at each time step, removing the cross-correlation step. This relieves the computational scaling from the harsh N_A^2 to the more gentle envelope of $\sim N_g \log_2 N_g$, where N_g is the number of grid points in the Fourier transform (e.g. Morales 2011; Tegmark & Zaldarriaga 2009; Tegmark & Zaldarriaga 2010). This architecture is often referred to as a “direct imaging” correlator because it eliminates the intermediate cross-correlation data products of the FX and XF correlators, but instead directly forms images from the electric field measurements.

Direct imaging correlators have begun to be explored on deployed arrays including the Basic Element for SKA Training II (BEST-2) array (Foster et al. 2014), the Omniscope (Zheng et al. 2014), and an earlier incarnation at higher frequencies with the intent of pulsar timing (Otoabe et al. 1994; Daishido et al. 2000). However, each of these examples make assumptions about the redundancy of the array layout, and require the collecting elements are identical. On the other hand, the MOFF algorithm achieves the same $N_g \log_2 N_g$ computational scaling without placing any restriction on antenna placement, can accommodate non-identical antennas, and is provably optimal (Morales 2011). This algorithm uses the antenna beam patterns to grid the electric field measurements to a regular grid in the software holography/A-transpose fashion (Morales & Matejek 2009; Bhatnagar, S. et al. 2008; Tegmark 1997a) before performing the spatial FFT. This process has been shown to theoretically produce a data product identical to images produced from traditional visibility-based techniques.

Here we present the first software implementation of the MOFF correlator, and announce the public release of the E-field Parallel Imaging Correlator (EPIC) code. EPIC is a highly parallel, object oriented Python package that primarily implements the MOFF imaging algorithm besides emulating real-life telescopes and FX/XF correlators in software, and includes a visibility-based imaging technique for reference. It is intended to provide a development platform to test different imaging approaches, characterize scaling relations and serve as a stepping stone for real-life GPU/FPGA-based implementation on telescopes.

We begin with a technical description of the algorithm in §2, then discuss our particular implementation in §3. We then verify the output data quality from our code in §4 by presenting simulated images from both the EPIC correlator and comparing to a simulated FX correlator. We also demonstrate the performance with real-world data from the LWA. §5 demonstrates its ability to robustly image data from heterogeneous arrays. In §6, we explore the scalability of the algorithm in the context of several array design choices. We identify specific array design classes where the EPIC correlator – is computationally more efficient; and in the field of transients, demands significantly lesser I/O bandwidth relative to visibility-based approaches. We conclude and discuss future research prospects in §7.

2 MATHEMATICAL FRAMEWORK

We provide a brief summary of the mathematical equivalence of the MOFF and FX correlators detailed in Morales (2011). We first relate the image produced from visibilities to the electric fields of astrophysical sources, then show that operations can be reordered to produce the same images at a lower computational cost.

Electric fields from astrophysical sources, $\mathcal{E}(\hat{\mathbf{s}}, f, t)$, in the sky coordinate system denoted by the unit vector $\hat{\mathbf{s}}$, propagate towards the observer as:

$$E(\mathbf{r}, f, t) = \int E(\hat{\mathbf{s}}, f, t) e^{-2\pi i f \mathbf{r} \cdot \hat{\mathbf{s}}/c} d\Omega, \quad (1)$$

where, \mathbf{r} denotes the observer’s location, f is the frequency of radiation, c is the speed of light, t denotes time and $E(\mathbf{r}, f, t)$ is the propagated electric field. Thus the propagated electric field is a linear superposition of the electric fields emanating from astronomical sources with appropriate complex phases. Ignoring wide-field effects, it can be simplified as a Fourier transform of the electric fields in the sky coordinates.

An antenna, located at \mathbf{r}_a (indexed by a), measures a phased sum of these propagated electric fields over its effective collecting area with an additive receiver noise:

$$E_a(f, t) = \int W_a(\mathbf{r} - \mathbf{r}_a, f, t) E(\mathbf{r}, f, t) d^2\mathbf{r} + n_a(f, t) \quad (2)$$

$$= \int W_a(\mathbf{r} - \mathbf{r}_a, f, t) \times \left[\int \mathcal{E}(\hat{\mathbf{s}}, f, t) e^{-2\pi i f \mathbf{r} \cdot \hat{\mathbf{s}}/c} d\Omega \right] d^2\mathbf{r} + n_a(f, t) \quad (3)$$

$$= \int W_a(\hat{\mathbf{s}}, f, t) \mathcal{E}(\hat{\mathbf{s}}, f, t) e^{-2\pi i f \mathbf{r}_a \cdot \hat{\mathbf{s}}/c} d\Omega + n_a(f, t) \quad (4)$$

where, $W_a(\mathbf{r}, f, t)$ is the aperture electric field illumination pattern of the antenna and its Fourier transform, $W_a(\hat{\mathbf{s}}, f, t)$, is the directional antenna voltage response at a given frequency and time.

Interferometers measure *visibilities* – the degree of coherence between electric fields measured by a pair of antennas (van Cittert 1934; Zernike 1938; Thompson et al. 2001).

A visibility, V_{ab} , can be written as:

$$\begin{aligned}
 V_{ab}(f, t) &= \langle E_a(f, t) E_b^*(f, t) \rangle_t \\
 &= \left\langle \left[\int \mathcal{W}_a(\hat{\mathbf{s}}, f, t) \mathcal{E}(\hat{\mathbf{s}}, f, t) e^{-2\pi i f \mathbf{r}_a \cdot \hat{\mathbf{s}}/c} d\Omega \right. \right. \\
 &\quad \left. \left. + n_a(f, t) \right] \right. \\
 &\quad \times \left[\int \mathcal{W}_b^*(\hat{\mathbf{s}}', f, t) \mathcal{E}^*(\hat{\mathbf{s}}', f, t) e^{2\pi i f \mathbf{r}_b \cdot \hat{\mathbf{s}}'/c} d\Omega' \right. \\
 &\quad \left. \left. + n_b^*(f, t) \right] \right\rangle_t \\
 &= \iint \mathcal{W}_a(\hat{\mathbf{s}}, f, t) \mathcal{W}_b^*(\hat{\mathbf{s}}', f, t) \left\langle \mathcal{E}(\hat{\mathbf{s}}, f, t) \mathcal{E}^*(\hat{\mathbf{s}}', f, t) \right\rangle_t \\
 &\quad \times e^{-2\pi i f (\mathbf{r}_a \cdot \hat{\mathbf{s}} - \mathbf{r}_b \cdot \hat{\mathbf{s}}')/c} d\Omega d\Omega' \\
 &\quad + \text{noise-like cross-terms.} \tag{5}
 \end{aligned}$$

where we have brought the time average into the integral under the assumption that the aperture illumination pattern does not change over the time-scale of the averaging and \star denotes complex conjugation. The noise-like cross-terms ideally have zero mean. This expression can be further simplified with the sky brightness, $\mathcal{I}(\hat{\mathbf{s}}, f, t) = \langle \mathcal{E}(\hat{\mathbf{s}}, f, t) \mathcal{E}^*(\hat{\mathbf{s}}', f, t) \rangle_t \delta(\hat{\mathbf{s}} - \hat{\mathbf{s}}')$, and defining the antenna-pair sky power response function (or the directional antenna-pair power pattern), $\mathcal{W}_{ab}(\hat{\mathbf{s}}) \equiv \mathcal{W}_a(\hat{\mathbf{s}}, f, t) \mathcal{W}_b^*(\hat{\mathbf{s}}, f, t)$. The result is the visibility expressed in terms of the sky brightness, the power pattern, and uncorrelated noise terms which we group into $n_{ab}(f, t)$.

$$\begin{aligned}
 V_{ab}(f, t) &= \int \mathcal{W}_{ab}(\hat{\mathbf{s}}, f, t) \mathcal{I}(\hat{\mathbf{s}}, f, t) e^{-2\pi i f \mathbf{r}_{ab} \cdot \hat{\mathbf{s}}/c} d\Omega \\
 &\quad + n_{ab}(f, t), \tag{7}
 \end{aligned}$$

where, the baseline coordinate $\mathbf{r}_{ab} \equiv \mathbf{r}_a - \mathbf{r}_b$ is the vector separation between the two antennas. This signifies that the visibility (V_{ab}) measured between a pair of antennas is obtained by the multiplying the sky brightness $\mathcal{I}(\hat{\mathbf{s}}, f, t)$ by the antenna power response $\mathcal{W}_{ab}(\hat{\mathbf{s}}, f, t)$ and Fourier transforming from the directional coordinates ($\hat{\mathbf{s}}$) to the **measurement plane**, which are then sampled at the locations of the antenna spacings (or baselines), namely, \mathbf{r}_{ab} , and added to the noise n_{ab} .

This can be equivalently re-written as:

$$\begin{aligned}
 V_{ab}(f, t) &= \int W_{ab}(\mathbf{r}_{ab} - \mathbf{r}, f, t) \\
 &\quad \times \left[\int \mathcal{I}(\hat{\mathbf{s}}, f, t) e^{-2\pi i f \mathbf{r} \cdot \hat{\mathbf{s}}/c} d\Omega \right] d^2\mathbf{r} + n_{ab}(f, t), \tag{8}
 \end{aligned}$$

where, $W_{ab}(\mathbf{r}, f, t)$ denotes the **power response of the antenna pair obtained in the measurement plane** by a spatial Fourier transform of $\mathcal{W}_{ab}(\hat{\mathbf{s}}, f, t)$. Effectively, the multiplication in image space by $\mathcal{W}_{ab}(\hat{\mathbf{s}}, f, t)$ has been replaced by a convolution with $W_{ab}(\mathbf{r}, f, t)$ in **measurement plane**. This is the software holographic equivalent of a traditional FX correlator output.

Hereafter, we adopt the matrix notation of Morales (2011), where vectors are represented with single coordinates, and matrices are represented by two coordinates denoting the spaces the operator transforms between. Since

each frequency is processed independently, we drop the dependence on f . In this notation, the above measurement equation can be expressed as:

$$\mathbf{m}(\mathbf{v}) = \mathbf{B}(\mathbf{v}, \mathbf{u}) \mathbf{F}(\mathbf{u}, \hat{\mathbf{s}}) \mathcal{I}(\hat{\mathbf{s}}) + \mathbf{n}(\mathbf{v}), \tag{9}$$

where the sky brightness $\mathcal{I}(\hat{\mathbf{s}})$ is Fourier transformed using $\mathbf{F}(\mathbf{u}, \hat{\mathbf{s}})$ and the resultant spatial coherence function is weighted and summed using the antenna power response, $\mathbf{B}(\mathbf{v}, \mathbf{u})$ in uv -space sampled at the baseline location to obtain the measured visibilities:

$$\mathbf{m}(\mathbf{v}) = \langle \mathbf{E}(\mathbf{a}) \mathbf{E}^*(\mathbf{a}') \rangle_t, \tag{10}$$

where $\mathbf{m}(\mathbf{v})$ denotes visibilities measured by cross-correlating measured antenna electric fields over all possible pairs of \mathbf{a} and \mathbf{a}' . It is the same as equation 5 written in matrix notation.

Using the optimal map-making formalism (Tegmark 1997b; Tegmark 1997a), a software holography image is formed using (Morales & Matejek 2009):

$$\mathcal{I}'(\hat{\mathbf{s}}) = \mathbf{F}^T(\hat{\mathbf{s}}, \mathbf{u}) \mathbf{B}^T(\mathbf{u}, \mathbf{v}) \mathbf{N}^{-1}(\mathbf{v}, \mathbf{v}) \mathbf{m}(\mathbf{v}) \tag{11}$$

where the measured visibilities are weighted by the inverse of the system noise, followed by a gridding process using the holographic antenna power response as the gridding kernel, followed by a Fourier transform to create an image $\mathcal{I}'(\hat{\mathbf{s}})$. This is the optimal estimate of the true image $\mathcal{I}(\hat{\mathbf{s}})$ given the visibility measurements.

The intermediate step of gridding with the antenna power response can be expressed as a convolution of a data vector generated by gridding the electric fields directly with the antenna illumination pattern.

$$\begin{aligned}
 \mathbf{B}^T(\mathbf{u}, \mathbf{v}) \mathbf{N}^{-1}(\mathbf{v}, \mathbf{v}) \mathbf{m}(\mathbf{v}) &= \left\langle \left[\mathbf{W}_a(\mathbf{r}, \mathbf{a}) \tilde{\mathbf{N}}^T(\mathbf{a}, \mathbf{a}) \mathbf{E}^*(\mathbf{a}) \right] \right. \\
 &\quad \left. * \left[\mathbf{W}_a^T(\mathbf{r}, \mathbf{a}) \tilde{\mathbf{N}}(\mathbf{a}, \mathbf{a}) \mathbf{E}(\mathbf{a}) \right] \right\rangle_t, \tag{12}
 \end{aligned}$$

where, \mathbf{N}^{-1} has been expressed as $\tilde{\mathbf{N}}^T \tilde{\mathbf{N}}$.

We can then use the multiplication-convolution theorem to move the convolution in Equation 12 to a square after the Fourier transform in equation 11.

$$\mathcal{I}'(\hat{\mathbf{s}}) = \left\langle \left| \mathbf{F}^T(\hat{\mathbf{s}}, \mathbf{r}) \mathbf{W}^T(\mathbf{r}, \mathbf{a}) \mathbf{N}^{-1}(\mathbf{a}, \mathbf{a}) \mathbf{E}(\mathbf{a}) \right|^2 \right\rangle_t. \tag{13}$$

The term inside the angular brackets before squaring has a very similar form as that in equation 11. It signifies that the measured antenna electric fields are weighted by the antenna noise, weighted and gridded by the antenna aperture kernel, Fourier transformed and finally squared to obtain the same image estimate that would have been obtained using equation 11.

Equation 13 is the optimal imaging equation used by the MOFF algorithm. While mathematically equivalent to equation 11, squaring in image space rather than convolving in uv space potentially saves orders of magnitude in computation.

There are some important differences between the two techniques:

- (i) The time-averaging cannot be performed on a stochastic measurement but only on its statistical properties. In visibility-based imaging, the visibilities measured between antenna pairs represent spatial correlations which can be

time-averaged followed by gridding and imaging. However, in MOFF imaging both antenna and gridded electric fields are stochastic and therefore must be imaged and squared before time-averaging.

(ii) In visibility-based imaging, electric fields measured by antennas are not correlated with themselves and hence lack zero spacing measurements. In contrast, in MOFF imaging, since the gridded electric fields are imaged and squared, they retain information from auto-correlated electric fields at zero spacing and thus yield the true total power of the imaged field.

3 SOFTWARE IMPLEMENTATION

We have implemented the MOFF imaging technique in our “E-field Parallel Imaging Correlator” – a highly parallelized Object Oriented Python package,² now publicly available. Besides implementing the MOFF imaging algorithm it also includes visibility-based imaging using the software holography technique and a simulator for generating electric fields from a sky model.

EPIC can accept dual-polarization inputs and produce images of all four instrumental cross-polarizations. Currently two data input formats exist for reading in the electric field time samples measured by the antennas – simulated electric fields based on a sky model using the simulator packaged with EPIC; and LWA data. Efforts to build interfaces for data from other telescopes are underway.

Fig. 1 shows the flowchart for MOFF imaging. The propagated electric fields are shown on the left at different time stamps, $t_1 \dots t_M$. At each time stamp, the electric fields measured by antennas are denoted by $\tilde{E}_1(t) \dots \tilde{E}_N(t)$. The F-engine performs a temporal Fourier transform on the electric field time-series to obtain electric field spectra $E_1(f) \dots E_N(f)$ ($\mathbf{E}(\mathbf{a})$ in matrix notation) for each of the antennas. Each of the complex antenna gains are calibrated to correct the corresponding electric field spectra. These calibrated electric fields are gridded using an antenna-based gridding convolution function after which it is spatially Fourier transformed and squared to obtain an image cube for every time stamp. These images are then time-averaged to obtain the accumulated image $\mathcal{I}'(f)$ ($\mathcal{I}(\hat{\mathbf{s}})$ in matrix notation).

Fig. 2 shows the flowchart for a visibility-based software holographic imaging from a FX correlator. The antenna-based F-engine is identical to that in the MOFF processing. The electric field spectra from each antenna are then cross-multiplied in the X-engine with those from all other antennas to obtain the visibilities $V_{ab}(f, t)$ ($\mathbf{m}(\mathbf{v})$ in matrix notation). They are calibrated and time-averaged to obtain $\langle V_{ab}(f) \rangle$ which are then gridded to obtain the image $\mathcal{I}'(f)$. The $\mathcal{I}'(f)$ obtained from both techniques are theoretically identical as explained in §2.

Here we discuss the components of these architectures in detail.

Antenna-to-Grid Mapping

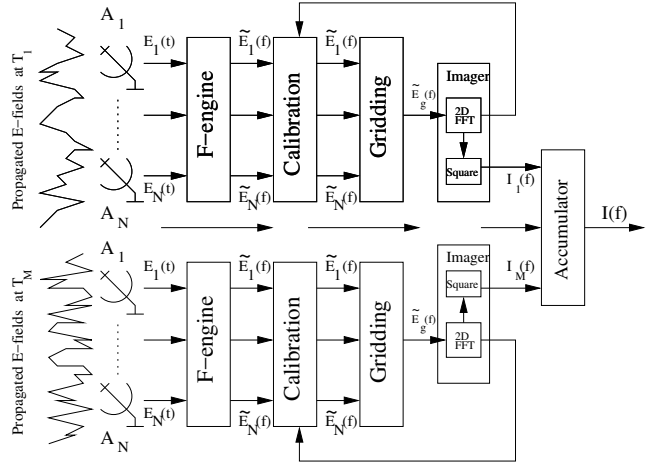


Figure 1. A flowchart of MOFF imaging in EPIC. The propagated electric fields shown on the left are measured as time-series $\tilde{E}_1(t) \dots \tilde{E}_N(t)$ by the antennas $A_1 \dots A_N$ which are then Fourier transformed by the F-engine to produce electric field spectra $E_1(f) \dots E_N(f)$. They are calibrated and gridded. The gridded electric fields $E_g(f)$ from each time series are imaged to produce images $\mathcal{I}'_1(f) \dots \mathcal{I}'_M(f)$. These images are time-averaged to obtain the final image $\mathcal{I}'(f)$.

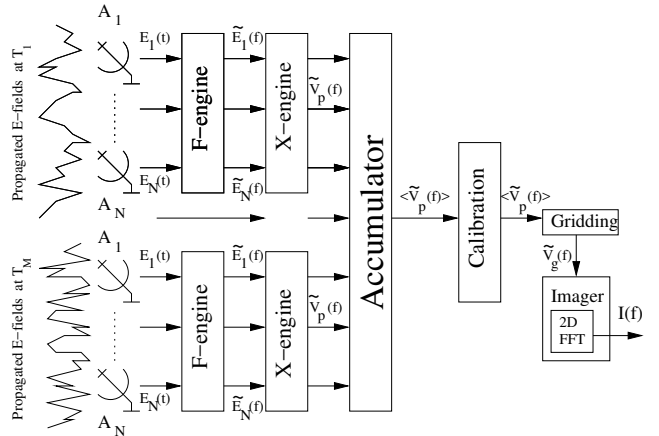


Figure 2. A flowchart of visibility-based software holographic imaging in EPIC. The FX process flow shares the F-engine with the MOFF process. Following the F-engine, the electric fields pass through the X-engine to produce visibilities $V_{ab}(f, t)$ which are calibrated and time-averaged. Then they are gridded to obtain the gridded visibilities $V_g(f)$ which are then Fourier transformed to obtain the image, $\mathcal{I}'(f)$.

A grid is generated on the coordinate system in which antenna locations are specified with a grid spacing. The grid spacing can be controlled by the user. By default, it is set to be $\leq \lambda/2$ even at the lowest wavelength to ensure there is no aliasing even from regions of the sky far away from the field of view. The number of locations on the grid is restricted to be a power of 2 for efficient use of FFT.

The gridding kernel in the simplest case is given by the antenna aperture illumination function, $W(\mathbf{r} - \mathbf{r}_a)$, which can be specified either by a functional form or as a table of values against locations around the antennas. A nearest neighbor mapping from all antenna footprints to grid locations is created using an efficient k-d tree algorithm

² The E-field Parallel Imaging Correlator (EPIC) package can be accessed at <https://github.com/nithyanandan/EPIC>

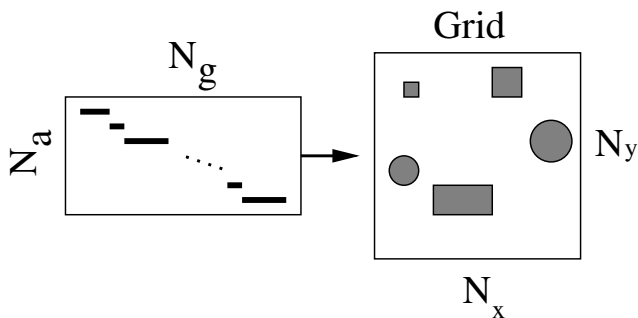


Figure 3. Block diagram of an antenna-to-grid mapping. A sparse block-diagonal matrix of total size $N_g \times N_a$ is created where each block contains roughly the number of pixels covered by the respective kernel. The antenna aperture illumination kernels do not have to be identical to each other. A discrete set of arbitrarily placed antennas are now placed on to a regular grid.

(Maneewongvatana & Mount 1999). There is no restriction here that the aperture illumination function has to be identical across antennas.

In the most general case, this gridding kernel could contain information on w -projection effects, and other time-dependent ionospheric effects. For a stationary antenna array in the absence of any time-dependent effects, this mapping must only be determined once in the antenna array coordinate frame. The antenna-to-grid mapping matrix, $\mathbf{M}(\mathbf{r}, \mathbf{a})$ is described as a transformation matrix from the space of measured electric fields by the antennas (\mathbf{a}) to the antenna array grid denoted by the coordinate \mathbf{r} . Since each antenna occupies a footprint typically the size of its aperture, $\mathbf{M}(\mathbf{r}, \mathbf{a})$, which is generally of size $N_g \times N_a$, reduces to a sparse block-diagonal matrix with only N_a blocks and roughly N_k non-zero entries per block, where N_k is the number of grid points that fall inside an antenna's footprint. This sparse matrix is stored in a Compressed Sparse Row (CSR) format. Fig. 3 illustrates the antenna-to-grid mapping matrix and the grid containing the mapped aperture footprints of the antennas.

Temporal Fourier transform

This module is common to the MOFF and visibility-based imaging techniques. Time samples of electric fields measured by the antenna and digitized by the A/D converter is Fourier transformed to generate electric field spectra. This step can be parallelized across antennas. The output is then fed to either MOFF or visibility-based imaging pipelines.

Calibration

Calibration of direct imaging correlators remains a challenge. Contrary to the FX data flow, direct imagers mix the signals from all antennas before averaging and writing to disk. It is therefore essential to apply gain solutions before the gridding step. Previous efforts have resorted to applying FX-generated calibration solutions (Zheng et al. 2014; Foster et al. 2014), or integrating a dedicated FX correlator which periodically forms the full visibility matrix (Wijnholds & van der Veen 2009; de Vos et al. 2009).

In a companion paper (Beardsley et al. 2016), we demonstrate a novel calibration technique (EPICal) which leverages the data products formed by direct imaging corre-

lators to estimate antenna complex gains. This method correlates the antenna electric field signals with an image pixel from the output of the correlator in the feedback calibration fashion outlined in Morales 2011 (illustrated in Fig. 1 by the arrow leading from the imager to the calibration block). Furthermore it allows for arbitrarily complex sky models, and following the MOFF algorithm places no restriction on array layout, and accounts for non-identical antenna beam patterns. Direction dependent calibration can be achieved by correlating antenna signals with output pixels in the direction of N_c calibration sources, then fitting for a functional model of the sky. Since antennas are only correlated with calibrator pixels, the computational complexity scales as $\sim N_a N_c$.

The calibration module included in EPIC allows for application of pre-determined calibration solutions, or can solve for the complex gains using the EPICal algorithm.

Gridding Convolution

The antenna array aperture illumination over the entire grid, $\mathbf{W}(\mathbf{r})$, is obtained by a projection of the individual antenna aperture illuminations:

$$\mathbf{W}(\mathbf{r}) = \sum_a \mathbf{W}_a(\mathbf{r} - \mathbf{r}_a), \quad (14)$$

or in matrix notation,

$$\mathbf{W}(\mathbf{r}) = \mathbf{M}(\mathbf{r}, \mathbf{a}) \mathbf{I}(\mathbf{a}), \quad (15)$$

where, $\mathbf{I}(\mathbf{a})$ is a row of ones denoting coverage of the grid by kernel footprints of antennas. This is achieved by efficient multiplication with the sparse matrix created in the antenna-to-grid mapping process using the sparse matrices module in Python SciPy package. Unless $\mathbf{W}(\mathbf{r})$ includes time-dependent effects of the ionosphere or the instrument, it needs to be computed just once for the entire observation. However, the gridding of electric fields must be computed at every readout of the electric field spectra,

$$\mathbf{E}(\mathbf{r}) = \mathbf{M}(\mathbf{r}, \mathbf{a}) \mathbf{E}(\mathbf{a}). \quad (16)$$

Spatial Fourier Transform

Before the spatial Fourier transform, the gridded electric fields are padded with zeros in order to match the grid size and angular size of each image pixel that would have been obtained with the software holography output from an FX correlator.

In MOFF imaging, these are spatially Fourier transformed followed by a squaring operation at every time stamp for every frequency channel. In visibility-based imaging, the spatial Fourier transform is performed only once per integration time-scale and does not include a squaring operation.

Time-averaging

In MOFF imaging, the measured antenna electric fields and the corresponding holographic electric field images are zero-mean stochastic quantities. Hence, they cannot be time-averaged to reduce noise. The statistical quantity stable with time in this case are the square of the holographic electric field images. Thus, squared images have to be formed at every instant of time before averaging as indicated in equation 13.

In contrast, visibilities measured by an antenna are statistically stable within an integration time interval. Hence, they are averaged after calibration as shown in equation 5. It is advantageous to average them in visibilities before imaging because the repeated cost of spatial FFT can be avoided. Since this averaging has been performed already on the visibilities over an integration time-scale, the imaging step has to be performed only once per integration cycle.

A high level software architecture of the EPIC package is described in the appendix §A for the interested reader.

4 VERIFICATION

In order to verify the accuracy of the EPIC code, we characterize the images produced through simulations. We simulate electric field streams from a model sky and process the data through both the MOFF and a visibility-based imaging algorithm. We then compare the output images to demonstrate their equivalence.

4.1 Simulations

We use the EPIC simulator to generate stochastic electric field samples from a sky model consisting of 10 point sources of random flux densities > 10 Jy each at random locations. In our simulations, we use 64 frequency channels each of width $\Delta f = 40$ kHz. The number of time stamps integrated in one integration cycle was kept at eight where each A/D timeseries is $1/\Delta f = 25 \mu\text{s}$ long. We use the MWA array layout (Beardsley et al. 2012) for demonstration. Only the inner 51 tiles within a square bounding box of 150 m on each side were used. We assumed all tiles are identical and have a square shaped electric field illumination footprint 4.4 m on each side. Besides the stochastic sky noise present in the simulated electric fields, no noise from the instrument is added.

4.2 Antenna auto-correlations

Before the outputs can be compared, we describe the elimination of a distinct difference between the two techniques. The squaring operation under MOFF imaging in the image plane introduces antenna auto-correlations around the zero spacing in the uv -plane which are absent in traditional visibility-based imaging. In order to facilitate a robust comparison between MOFF and visibility-based imaging techniques, these auto-correlations are removed from the MOFF algorithm output, which is otherwise not an essential part of the core algorithm. We describe below how they are removed.

The shape and extent of these auto-correlations can be estimated from the antenna aperture illumination pattern. The aperture illumination patterns are already available from the gridding step. Fig. 4 shows the estimated weights from antenna auto-correlations in the uv -plane (left) and the corresponding response in the image plane (right). The latter is simply the directional antenna power response.

We inverse Fourier transform the squared images and beams back to the uv plane and subtract the estimated auto-correlation kernel scaled to the peak value centred at the zero spacing pixel. The final averaged image is obtained by Fourier transforming the uv plane data and

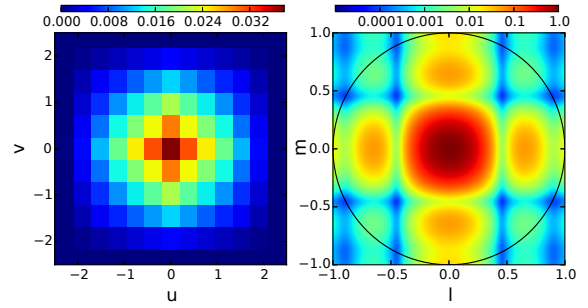


Figure 4. The auto-correlation of weights of a square shaped antenna aperture in the uv plane (left) and the corresponding directional antenna power response on the sky (right) in coordinates specified by direction cosines. The antenna auto-correlation weights are normalized to a sum of unity yielding a peak response of unity in the antenna’s directional power pattern on the sky. The color scale for the directional power pattern is logarithmic. The black circle indicates the sky horizon and values beyond it are not physical and hence ignored.

weights with the auto-correlations subtracted to the image plane. These images are now comparable to those obtained from visibility-based imaging. This step of removing auto-correlations needs to be performed only once per integration time-scale and does not add significant cost to the full operation.

4.3 Comparison of outputs

We investigate the two imaging algorithms for differences from the point of view of the quality of their outputs. We begin by comparing the images produced with the two approaches.

Fig. 5 shows the weighted dirty images (top) and synthesized beams (bottom) obtained with antenna-based MOFF and FX visibility-based imaging algorithms packaged in EPIC. The antenna auto-correlations that correspond to zero spacing have been removed from the correlated weights and data in the uv plane, the MOFF image and the corresponding synthesized beam as described in §4.2. The reconstructed sky image has the simulated sources at the expected sky positions in either case. Both algorithms result in images and synthesized beams that are well matched with each other. As expected, their fluxes are attenuated by a weighting proportional to the square of the antenna power pattern corresponding to a uniform square aperture.

We examine in detail the respective synthesized beams in each case in Fig. 6. Slices at $m = 0$ of the synthesized beams weighted by the antenna power pattern are shown for MOFF method using EPIC (solid black) and visibility-based (dashed gray) imaging. The two are found to match well. A magnified view shows that some differences at the level of $< 0.5\%$ exist in some regions. These are attributed to differences in the uv -plane antenna cross-correlation weights in the two methods which in turn arises due to the amount of coarseness in grid spacing as described below.

The left panel of Fig. 7 shows differences (in percentage relative to peak) in cross-correlated weights obtained with MOFF imaging in EPIC and visibility-based imaging. The maximum difference appears near the center of the uv -plane

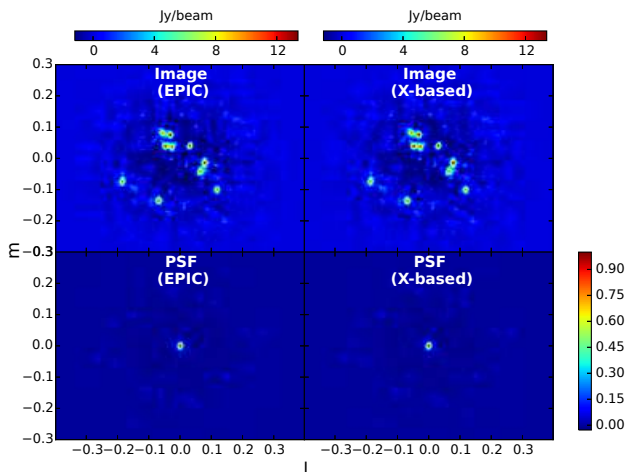


Figure 5. Weighted dirty images (top) and synthesized beams (bottom) obtained from simulated data using EPIC implementation of antenna-based MOFF algorithm (left) and visibility-based imaging (right). The antenna auto-correlations at zero-spacing have been removed from the MOFF images. The images in either case reconstruct the sources at the right locations with the fluxes attenuated expected after multiplication by the antenna power pattern. The synthesized beams from the two algorithms are well matched in size and shape. The overall modulation by the power pattern is seen clearly in both images.

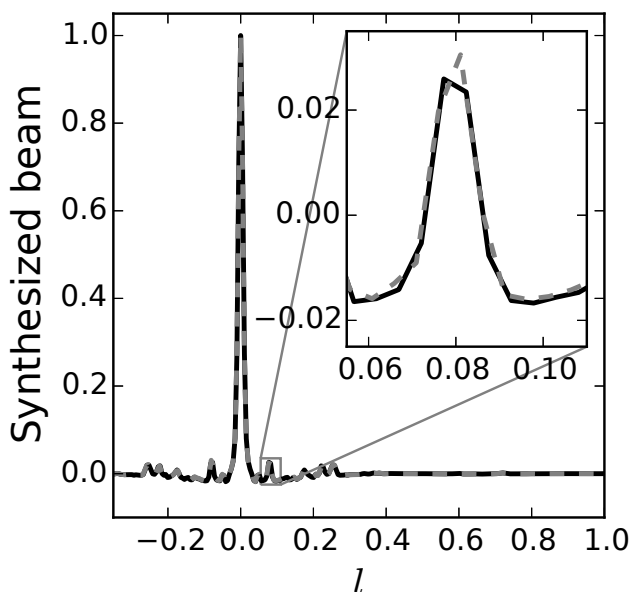


Figure 6. Synthesized beams weighted by antenna power pattern sliced at $m = 0$ obtained with MOFF algorithm using EPIC (solid black line) and visibility-based imaging (dashed gray line). The two appear almost identical. The inset provides a magnified view of differences in the synthesized beam slices between the two techniques at levels $\lesssim 0.5\%$ relative to the peak. These are attributed to differences that arise in gridding and depends on the coarseness of the grid.

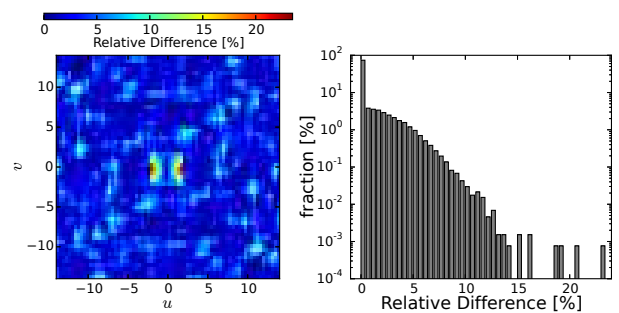


Figure 7. *Left:* Differences (in %) in cross-correlated weights in the uv plane relative to the peak. The biggest difference ($\sim 20\%$) is found around the zero-spacing corresponding to auto-correlations of antenna weights due to gridding differences augmented by the relatively high number density of antenna auto-correlation footprints in that region. In most of the other regions, differences of the order of less than a few percent are seen. *Right:* Histogram (expressed as percentage) of the relative differences (in %) between antenna cross-correlation weights shown on the left binned in intervals of 0.5% . Over 70% of the uv -cells do not differ by more than 0.5% and over 90% of uv -cells only differ by $< 5\%$ for the gridding coarseness used.

corresponding to antenna auto-correlations which have not been perfectly removed in the former. In other regions of the uv -plane, the differences are of the order of a few percent. The reason for these differences is described below.

The gridding step in MOFF imaging samples the antenna footprint (either in analytic or lookup table formats) at the grid locations. Coverage of grid pixels by an antenna footprint may be ~ 1 pixel narrower particularly at the edge of the footprint along one or both directions relative to that from another identical antenna but with a fractionally different location relative to the grid. This depends on the exact location of the centre of the antenna relative to the grid and the coarseness of grid spacing. This first order loss of precision of the sampled footprint propagates to second order (~ 2 pixels) upon correlation of the discretized weights. In other words, the correlated weights may suffer further loss of precision in their sampled footprint after correlation of two footprints each of which could be less precise to first order. On the other hand, in visibility-based imaging, a directly sampled uv plane antenna power response (which is theoretically identical to the correlation of individual antenna footprints) centred on a baseline has a loss in precision at most to first order. Thus, although in the limit of infinitesimally small grid spacing they should be identical, the coarseness of grid spacing introduces subtle differences between the two.

These differences which are dependent on the coarseness of grid spacing can be mitigated by making the grid spacing finer at the expense of increased computational cost. Residuals centred around zero spacing can also be lowered by subtracting each auto-correlation of antenna weights separately by using the shape and extent of the sampled footprint appropriate for that specific antenna aperture. This is a general solution applicable even in case of heterogeneous antenna arrays and is under active development for EPIC.

We study the effect of the differences in gridded weights on the image plane. Fig. 8 shows the difference between the

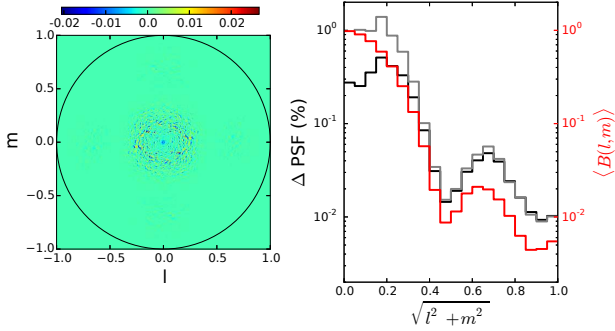


Figure 8. Map of difference between the synthesized beams obtained with the two methods (left) and radial statistics of the synthesized beams and their differences (right). The radial variations of rms of the synthesized beam (gray) and that of the rms of the difference (black) are shown as percentage of the peak synthesized beam. Radially averaged directional antenna power response in absolute scale is shown in red and is to be read with the scale on the right side of the axis. The maximum difference is of the order of a few percent. Amplitude of the rms of the difference is modulated by the power pattern of the antenna.

synthesized beams obtained with the two methods. A difference map between the two synthesized beams is shown on the left. The amplitude of the difference appears to be modulated by the directional power response of the antenna. On the right, in radial bins, the rms of the synthesized beam (gray) and the rms of the difference map (black) are plotted in percentage units relative to the peak (to be read using the axis on the left side of the plot). The antenna power pattern (red; to be read using the scale on the right) is plotted for reference.

The synthesized beam rms is proportional to the antenna power pattern as expected from a point spread function uncorrected for the antenna power pattern. The rms of differenced synthesized beams is also modulated by the antenna power pattern. The rms of the difference is definitely lesser than the rms of the synthesized beam in the central regions up to $(l^2 + m^2)^{1/2} \lesssim 0.3$. This implies that the beams are well matched in the central regions. In the outer regions, their mismatch is comparable to the rms of synthesized beams. These findings are consistent with Fig. 6. This indicates the two synthesized beams are not randomly different from each other in which case the rms of the difference would have been $\approx \sqrt{2}$ higher than the rms of the each of the synthesized beams. This means that while differences exist, large fractions of them are still well matched to each other even out to the horizon. Thus the rounding errors in gridding do not affect the statistics of the images or the synthesized beams.

4.4 Application to LWA data

Here we demonstrate our software using narrow band data from the LWA station in New Mexico. This data is in LWA narrow-band transient buffer (TBN) format from 255 antennas within roughly a diameter of 100 m. The data is centred at a frequency of 74.03 MHz, with a sample rate (equal to the bandwidth) of 100 kHz with 512 complex time samples per antenna in a A/D writeout time-scale of 5.12 ms, a frequency

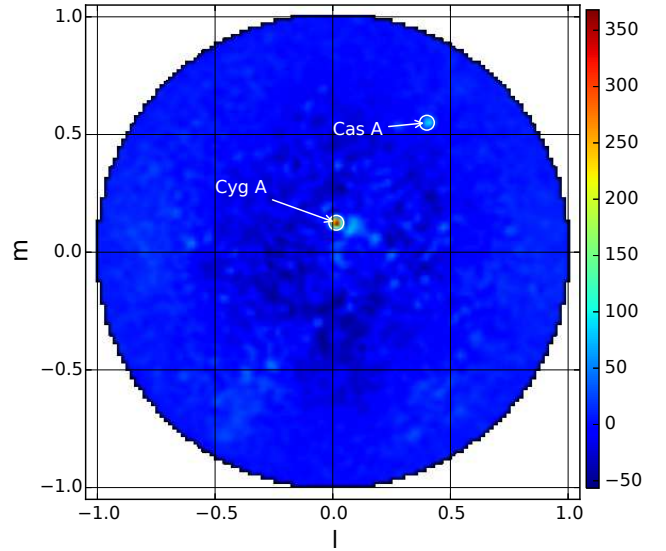


Figure 9. Image from LWA TBN data obtained with MOFF imaging using EPIC package after averaging over 20 ms and ≈ 80 kHz. The x- and y-axes denote direction cosines l and m respectively. The antenna voltages are compensated for their respective delays. The flux scale is arbitrary. Locations of Cyg A and Cas A are annotated.

resolution of 195.3125 Hz and dual polarization. There are 391 such writeouts (or time stamps; each contains 512 time samples at 100 kHz sampling) yielding a total duration of 2 s.

We corrected the cable delays, but otherwise assume the data is sufficiently calibrated to image directly. A detailed demonstration of EPICal on this data is presented in Beardsley et al. (2016).

Fig. 9 shows the image produced with MOFF imaging packaged in EPIC after averaging over ≈ 20 ms (four writeouts) of data and the inner ≈ 80 per cent of bandwidth (roughly 80 kHz). The image is shown in direction cosine coordinates l along the horizontal axis and m along the vertical axis. The flux scale is arbitrary. Even in this proof-of-concept demonstration, we see Cyg A and Cas A prominently as annotated, thus validating the functionality of EPIC.

5 IMAGING WITH HETEROGENEOUS ANTENNA ARRAYS

One of the advanced features of the MOFF algorithm and its implementation via EPIC is the ability to naturally account for heterogeneity of antennas while still producing images with maximal information (Morales 2011). Unlike the assumption frequently made in standard radio interferometry that all antennas are identical, EPIC can implement the most generic case where no such assumption can be made. In other words, EPIC does not assume $W_a(\mathbf{r} - \mathbf{r}_a)$ or $W_{ab}(\mathbf{r} - \mathbf{r}_{ab})$ for different antennas are identical. However, any *a priori* knowledge available that certain sets of antennas have identical illumination patterns can be easily

passed on to EPIC to avoid redundant computations and thus increase efficiency.

We present a methodology to understand the effective angular weighting in the image obtained with EPIC from a heterogeneous array and compare it with that from standard interferometry that assumes a homogeneous array (all antennas are identical). We also demonstrate how the assumption in the latter results in a mis-estimation of the recovered sky model.

Dropping the noise term and time dependence, the visibility measured by an antenna pair can be written from equation 7 as:

$$V_{ab}(f) = \int \mathcal{W}_a^I(\hat{s}, f) \mathcal{W}_b^{I*}(\hat{s}, f) \mathcal{I}(\hat{s}, f) e^{-2\pi i f \mathbf{r}_{ab} \cdot \hat{s}/c} d\Omega, \quad (17)$$

where, superscript ‘I’ in the \mathcal{W} term indicates the weighting is inherently introduced by the instrument during the measurement process. The beam-weighted dirty image is:

$$\mathcal{I}_D(\hat{s}, f) = \frac{1}{N_A(N_A - 1)/2} \sum_{ab} V_{ab}(f) e^{2\pi i f \mathbf{r}_{ab} \cdot \hat{s}/c}. \quad (18)$$

When the array is homogeneous, $\mathcal{W}^I \equiv \mathcal{W}_a^I \equiv \mathcal{W}_b^I$ and the above equation reduces to:

$$\mathcal{I}_D(\hat{s}, f) = |\mathcal{W}^I(\hat{s}, f)|^2 \mathcal{I}_D^{\text{iso}}(\hat{s}, f), \quad (19)$$

where, $\mathcal{I}_D^{\text{iso}}(\hat{s}, f)$ is the dirty image with no beam weighting (isotropic uniform weighting) determined only by the array layout and $|\mathcal{W}^I|^2$ is the directional power pattern of the antenna pair familiar in standard interferometry.

While imaging, EPIC introduces a weighting to each antenna during gridding as given by equations 11 and 12, and equivalently, the weighted visibility from antenna pair ab projected on the grid is:

$$V'_{ab}(\mathbf{r}, f) = B_{ab}^{G*}(\mathbf{r} - \mathbf{r}_{ab}, f) V_{ab}, \quad (20)$$

where, $B_{ab}^G(\mathbf{r} - \mathbf{r}_{ab}, f)$ is obtained by the spatial cross-correlation of weighting kernels associated with the individual antennas using the definition:

$$B_{ab}^G(\mathbf{r} - \mathbf{r}_{ab}, f) = \int W_a^G(\mathbf{r}' - \mathbf{r}_a) W_b^{G*}(\mathbf{r}' + \mathbf{r} - \mathbf{r}_b) d^2\mathbf{r}'. \quad (21)$$

The superscript ‘G’ denotes the weighting introduced in analysis during the gridding process. Optimal imaging requires $W_a^G = W_a^I$ (Morales & Matejek 2009; Morales 2011). However, we keep the two superscripts separately to describe output images under the wrong assumption that the array is homogeneous when instead it is actually heterogeneous.

The sky response of the weighted visibility is:

$$\begin{aligned} \mathcal{I}'_{ab}(\hat{s}, f) &= \int V'_{ab}(\mathbf{r}, f) e^{2\pi i f \mathbf{r} \cdot \hat{s}/c} d^2\mathbf{r} \\ &= \int B_{ab}^{G*}(\mathbf{r} - \mathbf{r}_{ab}, f) V_{ab} e^{2\pi i f \mathbf{r} \cdot \hat{s}/c} d^2\mathbf{r} \\ &= V_{ab} \int \left[\int W_a^{G*}(\mathbf{r}' - \mathbf{r}_a) W_b^G(\mathbf{r}' + \mathbf{r} - \mathbf{r}_b) d^2\mathbf{r}' \right] \\ &\quad \times e^{2\pi i f \mathbf{r} \cdot \hat{s}/c} d^2\mathbf{r} \\ &= \mathcal{W}_a^{G*}(\hat{s}, f) \mathcal{W}_b^G(\hat{s}, f) V_{ab} e^{2\pi i f \mathbf{r}_{ab} \cdot \hat{s}/c}, \end{aligned} \quad (22)$$

which denotes the fringe from the weighted visibility. The

image output of EPIC is equivalent to averaging these weighted fringes from all antenna pairs:

$$\begin{aligned} \mathcal{I}'(\hat{s}, f) &= \frac{1}{N_A(N_A - 1)/2} \sum_{\substack{ab \\ a \neq b}} \mathcal{I}'_{ab}(\hat{s}, f) \\ &= \frac{1}{N_A(N_A - 1)/2} \sum_{\substack{ab \\ a \neq b}} \left[\mathcal{W}_a^{G*}(\hat{s}, f) \mathcal{W}_b^G(\hat{s}, f) V_{ab} \right. \\ &\quad \left. \times e^{2\pi i f \mathbf{r}_{ab} \cdot \hat{s}/c} \right]. \end{aligned} \quad (23)$$

If all antennas are identically weighted ($W^G \equiv W_a^G \equiv W_b^G$), using equation 19, equation 23 reduces to:

$$\begin{aligned} \mathcal{I}'(\hat{s}, f) &= \frac{|\mathcal{W}^G(\hat{s}, f)|^2}{N_A(N_A - 1)/2} \sum_{\substack{ab \\ a \neq b}} V_{ab} e^{2\pi i f \mathbf{r}_{ab} \cdot \hat{s}/c} \\ &= |\mathcal{W}^G(\hat{s}, f)|^2 \mathcal{I}_D(\hat{s}, f) \\ &= |\mathcal{W}^G(\hat{s}, f)|^2 |\mathcal{W}^I(\hat{s}, f)|^2 \mathcal{I}_D^{\text{iso}}(\hat{s}, f). \end{aligned} \quad (24)$$

Thus, the dirty image, which is already attenuated by the instrumental power pattern, gets further attenuated by the power pattern introduced in the gridding step in EPIC imager. This is consistent with Morales & Matejek (2009).

We consider a heterogeneous array consisting of a total of N_A antennas under N_T different types. And under each antenna type i , there are n_i antennas such that $\sum_i n_i = N_A$. The total number of unique non-zero spacing antenna pairs is $N_A(N_A - 1)/2$ and there are potentially $N_T(N_T + 1)/2$ unique antenna pair types obtained by pairwise combination of the N_T antenna types. Thus,

$$\frac{1}{2} N_A(N_A - 1) = \frac{1}{2} \sum_{i=1}^{N_T} \sum_{\substack{j=1 \\ i \neq j}}^{N_T} n_i n_j + \frac{1}{2} \sum_{i=1}^{N_T} n_i(n_i - 1) \quad (25)$$

is obtained by counting antenna pairs from different antenna types (first term) and those from the same antenna type (second term).

Since equation 23 is obtained by averaging weighted fringes over all unique antenna pairs, it can be expressed as:

$$\begin{aligned} \mathcal{I}'(\hat{s}, f) &= \frac{1}{N_A(N_A - 1)/2} \left[\frac{1}{2} \sum_{i=1}^{N_T} \sum_{\substack{j=1 \\ i \neq j}}^{N_T} \sum_{\substack{ab \\ a \neq b \\ a \in i, b \in j}} \mathcal{I}'_{ab}(\hat{s}, f) \right. \\ &\quad \left. + \frac{1}{2} \sum_{i=1}^{N_T} \sum_{\substack{ab \\ a \neq b \\ a, b \in i}} \mathcal{I}'_{ab}(\hat{s}, f) \right]. \end{aligned} \quad (26)$$

Here, equation 23 has been decomposed as the sum of fringes over all unique antenna pairs in an antenna pair type (innermost summation) and subsequently summed over all antenna pair types.

In order to simplify the analysis, we assume that the spatial distribution of antenna pairs in each antenna pair type are similar and thus result in a similar dirty image, $\mathcal{I}_D^{\text{iso}}(\hat{s}, f)$. This usually holds when N_A is large and antennas under each antenna type are chosen randomly such that

differences in the point spread functions are insignificant. Under this assumption, equation 26 can be written as:

$$\begin{aligned} \mathcal{I}'(\hat{s}, f) \approx & \frac{\mathcal{I}_D^{\text{iso}}(\hat{s}, f)}{N_A(N_A - 1)/2} \\ & \times \left[\frac{1}{2} \sum_{i=1}^{N_T} \sum_{j=1}^{N_T} \sum_{\substack{ab \\ a \neq b \\ a \in i, b \in j}} \left\{ \mathcal{W}_a^{G*}(\hat{s}, f) \mathcal{W}_b^G(\hat{s}, f) \right. \right. \\ & \left. \left. \times \mathcal{W}_a^I(\hat{s}, f) \mathcal{W}_b^{I*}(\hat{s}, f) \right\} \right. \\ & \left. + \frac{1}{2} \sum_{i=1}^{N_T} \sum_{\substack{ab \\ a \neq b \\ a, b \in i}} \left\{ \mathcal{W}_a^{G*}(\hat{s}, f) \mathcal{W}_b^G(\hat{s}, f) \right. \right. \\ & \left. \left. \times \mathcal{W}_a^I(\hat{s}, f) \mathcal{W}_b^{I*}(\hat{s}, f) \right\} \right], \end{aligned} \quad (27)$$

where, $\mathcal{I}_D^{\text{iso}}(\hat{s}, f)$ is approximately the same for all terms and has been pulled outside the summations. For all antennas indexed by a that belong to a particular type i , we replace \mathcal{W}_a with $\mathcal{W}_{(i)}$ that arise from both instrumental (superscript ‘ I ’) and gridding (superscript ‘ G ’) origins. Using arguments similar to those in equation 25, equation 27 can be further simplified to:

$$\begin{aligned} \mathcal{I}'(\hat{s}, f) \approx & \frac{\mathcal{I}_D^{\text{iso}}(\hat{s}, f)}{N_A(N_A - 1)/2} \\ & \times \left[\frac{1}{2} \sum_{i=1}^{N_T} \sum_{j=1}^{N_T} n_i n_j \left\{ \mathcal{W}_{(i)}^{G*}(\hat{s}, f) \mathcal{W}_{(j)}^G(\hat{s}, f) \right. \right. \\ & \left. \left. \times \mathcal{W}_{(i)}^I(\hat{s}, f) \mathcal{W}_{(j)}^{I*}(\hat{s}, f) \right\} \right. \\ & \left. + \frac{1}{2} \sum_{i=1}^{N_T} n_i(n_i - 1) \left| \mathcal{W}_{(i)}^G(\hat{s}, f) \right|^2 \left| \mathcal{W}_{(i)}^I(\hat{s}, f) \right|^2 \right]. \end{aligned} \quad (28)$$

Then the effective attenuation of the dirty image due to instrumental and gridding weights is:

$$\mathcal{W}_{\text{eff}} = \mathcal{I}'(\hat{s}, f) / \mathcal{I}_D^{\text{iso}}(\hat{s}, f). \quad (29)$$

This means that the effective attenuation of the dirty image is obtained by combinations of the fourth power of antenna voltage patterns each weighted by the number of antenna pairs in those antenna pair types. In an optimally weighted

image, $\mathcal{W}_{(i)}^G \equiv \mathcal{W}_{(i)}^I$ and thus, equation 29 reduces to:

$$\begin{aligned} \mathcal{W}_{\text{eff}}^{\text{opt}} \approx & \frac{1}{N_A(N_A - 1)/2} \\ & \times \left[\frac{1}{2} \sum_{i=1}^{N_T} \sum_{j=1}^{N_T} n_i n_j \left| \mathcal{W}_{(i)}^I(\hat{s}, f) \right|^2 \left| \mathcal{W}_{(j)}^I(\hat{s}, f) \right|^2 \right. \\ & \left. + \frac{1}{2} \sum_{i=1}^{N_T} n_i(n_i - 1) \left| \mathcal{W}_{(i)}^I(\hat{s}, f) \right|^4 \right], \end{aligned} \quad (30)$$

where the superscript ‘opt’ denotes ‘optimal’.

For purposes of illustration, we consider a simple scenario in which there are two antenna types each containing roughly equal numbers of antennas with similar layouts but the analysis is performed under the wrong assumption that all antennas are identical and are all of the first type. In an optimally weighted image, the optimal effective weighting given by equation 29 will be:

$$\begin{aligned} \mathcal{W}_{\text{eff}}^{\text{opt}} \approx & \frac{1}{N_A(N_A - 1)} \left[n_1 n_2 \left| \mathcal{W}_{(1)}^I(\hat{s}, f) \right|^2 \left| \mathcal{W}_{(2)}^I(\hat{s}, f) \right|^2 \right. \\ & + n_1(n_1 - 1) \left| \mathcal{W}_{(1)}^I(\hat{s}, f) \right|^4 \\ & \left. + n_2(n_2 - 1) \left| \mathcal{W}_{(2)}^I(\hat{s}, f) \right|^4 \right]. \end{aligned} \quad (31)$$

On the other hand, $\mathcal{W}_{(1)}^G(\hat{s}, f) = \mathcal{W}_{(1)}^I(\hat{s}, f)$ and $\mathcal{W}_{(2)}^G(\hat{s}, f) = \mathcal{W}_{(1)}^I(\hat{s}, f)$ for an image obtained in the erroneous case in which all antennas are assumed to be identical. It will be sub-optimal whose effective weighting will be:

$$\begin{aligned} \mathcal{W}_{\text{eff}}^{\text{sub}} \approx & \frac{1}{N_A(N_A - 1)} \left[\left\{ n_1 n_2 \left| \mathcal{W}_{(1)}^I(\hat{s}, f) \right|^2 \right. \right. \\ & \left. \left. \times \mathcal{W}_{(1)}^I(\hat{s}, f) \mathcal{W}_{(2)}^{I*}(\hat{s}, f) \right\} \right. \\ & + n_1(n_1 - 1) \left| \mathcal{W}_{(1)}^I(\hat{s}, f) \right|^4 \\ & + n_2(n_2 - 1) \left| \mathcal{W}_{(1)}^I(\hat{s}, f) \right|^2 \\ & \left. \times \left| \mathcal{W}_{(2)}^I(\hat{s}, f) \right|^2 \right]. \end{aligned} \quad (32)$$

Finally, since no *a priori* information will be available about the heterogeneous array in case of the erroneous assumption, the effective weighting in the image will be believed to be $\mathcal{W}_{\text{eff}}^{\text{err}} = \left| \mathcal{W}_{(1)}^I \right|^4$.

Estimates of the dirty images with uniform, isotropic weighting in the optimal and erroneous cases will be obtained by dividing the respective weighted images by their assumed effective weights $\mathcal{W}_{\text{eff}}^{\text{opt}}$ and $\mathcal{W}_{\text{eff}}^{\text{err}}$ respectively as:

$$\hat{\mathcal{I}}_D^{\text{iso}} \approx \begin{cases} \mathcal{I}_D^{\text{iso}} & , \quad \text{optimal case} \\ \mathcal{I}_D^{\text{iso}} \frac{\mathcal{W}_{\text{eff}}^{\text{sub}}}{\mathcal{W}_{\text{eff}}^{\text{err}}} & , \quad \text{erroneous case} \end{cases} \quad (33)$$

If $\mathcal{I}_M(\hat{s}, f)$ is the sky model, then $\hat{\mathcal{I}}_D^{\text{iso}}(\hat{s}, f)$ can be expressed as:

$$\hat{\mathcal{I}}_D^{\text{iso}}(\hat{s}, f) = \mathcal{I}_M(\hat{s}, f) + \delta \mathcal{I}_S(\hat{s}, f) + \delta \mathcal{I}_M(\hat{s}, f), \quad (34)$$

where the second and third terms on the right hand side

denote fluctuations due to sidelobes and those intrinsic to the model, respectively. We define the normalized estimates of the sky model $\hat{\mathcal{I}}_{\text{M}}^{\text{norm}} \equiv \hat{\mathcal{I}}_{\text{D}}^{\text{iso}}/\mathcal{I}_{\text{M}}$. Ideally, $\hat{\mathcal{I}}_{\text{M}}^{\text{norm}}$ should be consistent with unity and not exceed beyond levels of uncertainty as determined by equation 34.

In our simulations, the antenna layout, duration of observation, center frequency and bandwidth used are the same as in §4.1. Antennas have square apertures. Those of the first and second types, which have roughly equal numbers of antennas with similar layouts, have 1.1 m and 6.6 m on their sides respectively. $\mathcal{I}_{\text{M}}(\hat{s}, f)$ consists of point sources of random flux densities brighter than 10 Jy along westward and south-westward directions as seen in Fig. 10a, which shows an optimally weighted image, $\mathcal{I}'(\hat{s}, f)$, obtained with EPIC using the MOFF algorithm after averaging over the entire bandwidth and duration of simulated observation.

$\hat{\mathcal{I}}_{\text{D}}^{\text{iso}}$ was estimated at the point source locations while the sidelobe levels were estimated from boxes three times bigger on the side than those shown using the ‘median absolute deviation’ metric which is resistant to outliers (other point sources in the sky model in our case). The intrinsic fluctuations in the modeled point sources were obtained statistically over time. The net uncertainty was determined by adding the levels of sidelobe fluctuations and intrinsic source fluctuations in quadrature. The normalized estimates of the sky model, $\hat{\mathcal{I}}_{\text{M}}^{\text{norm}}$, and the corresponding “1 σ ” error bars were obtained by dividing $\hat{\mathcal{I}}_{\text{D}}^{\text{iso}}$ and the net uncertainty by the respective effective weights in either case.

Fig. 10b shows $\hat{\mathcal{I}}_{\text{M}}^{\text{norm}}$ including the uncertainty as a function of distance from the center of the image. The gray and red bands denote estimates from the optimal and the erroneous cases, respectively. The solid and dashed lines correspond to point sources in the south-westward and westward directions respectively. It can be clearly seen that the estimates in the optimal case in almost all parts of the image are consistent with unity to within 1 σ . In complete contrast, in the erroneous case, the estimated values appear to be underestimated and deviate from the ideal value of unity with very high significance ($\gtrsim 5\sigma$) in most parts of the image. The reason for underestimation is because nearly half the antennas are assumed to be smaller than they actually are and thus results in dividing by overestimated $\mathcal{W}_{\text{eff}}^{\text{err}}$. These trends do not seem to be affected by the placement of sources along westward and south-westward directions.

This demonstrates that images from EPIC can robustly image data from heterogeneous arrays while being mathematically optimal. Besides being sub-optimal, erroneous assumptions about the homogeneity of an array can lead to significant and systematic mis-estimates (in this case, an underestimate) of the sky model.

6 ANALYSIS AND FEASIBILITY

We now investigate the feasibility of implementing the EPIC imager on current and future radio telescopes.

6.1 Processing Volumes

We have profiled the core routines of EPIC line-by-line for various ranges of parameters such as antenna filling fraction,

maximum baseline length, bandwidth and frequency resolution, integration time-scale, etc. for HERA antenna layouts which are highly compact. However, we note that in general, the hardware and optimization of routines in place will determine the relative speeds of the different stages in the pipeline.

Of all steps in the MOFF pipeline that are repeated for every writeout from the F-engine, the most expensive step even for dense HERA layouts is found to be the spatial two-dimensional FFT in the imaging stage relative to applying the sparse matrix gridding convolution, squaring or time-averaging. For instance, even in the conservative dense array layout scenario that makes these other stages even more expensive, the gridding convolution, squaring and time-averaging take up only $\lesssim 20\%$, $\lesssim 20\%$ and $\lesssim 5\%$ respectively of the total processing time while the spatial Fourier transform takes up $\gtrsim 55$ per cent of the total time. With sparser arrays the gridding process will be even faster.

In visibility-based imaging, the predominant computational cost is at the X-engine requiring $N_{\text{A}}(N_{\text{A}} - 1)/2$ complex multiplications per channel at every A/D writeout time-scale.

In the following discussions, we will assume that the computational cost for the MOFF imaging is determined by the spatial Fourier transform while that for visibility-based imaging comes from the cross-correlations. However, if non-linearities such as non-coplanarity of baselines (Cornwell et al. 2008) and wide-field phenomena like the *pitchfork* effect (Thyagarajan et al. 2015a,b) are to be corrected for, the antenna illumination footprint will become less compact in the measurement plane and can result in a costlier gridding process.

The number of complex multiplications and additions in the spatial Fourier transform implemented via FFT is $\approx \beta (4N_{\text{g}}) \log_2(4N_{\text{g}})$ where N_{g} is the number of pixels on the grid, the factor 4 accounts for increase in number of pixels as a result of zero-padding before spatial Fourier transform, and β is a constant that depends on the implementation of twiddle FFT algorithms (Brigham 1974). In our study, we set $\beta = 5$, a value³ much more conservative than was indicated in Morales (2011). We set the number of complex multiplications in the X-engine in visibility-based imaging to $N_{\text{A}}(N_{\text{A}} - 1)/2$.

We consider a variety of current and planned radio telescopes. Their antenna layouts are summarized in Table 1. The size of the layout gives the maximum baseline b_{max} . The grid spacing is determined by the science goals of the experiment in general. For our purpose, we assume a typical requirement that only the field of view of the antenna is to be imaged. This sets the grid spacing to be equal to the size of the antenna, A_{a} . Hence, $N_{\text{g}} \simeq b_{\text{max}}^2/A_{\text{a}}$.

Fig. 11 shows the number of complex operations per frequency channel per cross-polarization per integration time-scale. Telescopes that fall to the left of the solid line indicate MOFF imaging is computationally more efficient than visibility-based imaging. All HERA layouts except HERA-19 and HERA-37 are in a region of parameter space where MOFF imaging holds the advantage. The dashed line show-

³ <http://www.fftw.org/speed/method.html>

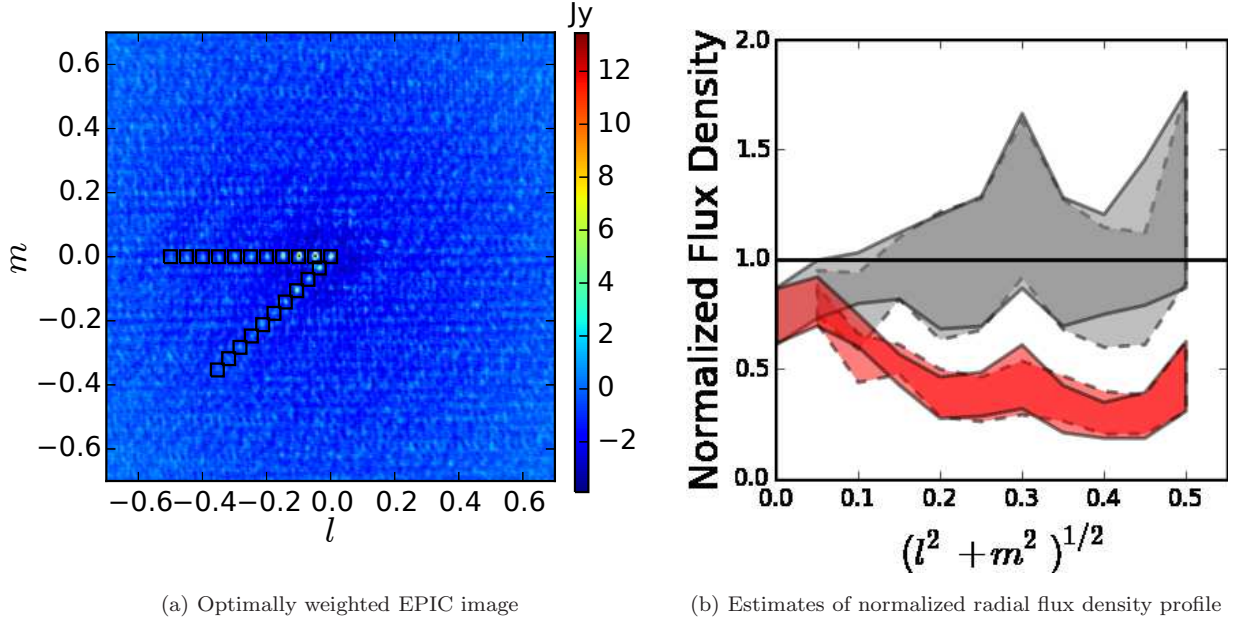


Figure 10. (a) Optimally weighted image, $\mathcal{I}'(\hat{s}, f)$, of simulated sky model obtained by EPIC using MOFF algorithm after averaging over entire bandwidth and duration of simulated observation. 51 antennas in the inner core of the MWA layout were used with uniformly illuminated square apertures. Roughly half of them were squares with 1.1 m sides (first type) and the rest with 6.6 m (second type). Point sources were simulated along westward and south-westward directions with random flux densities brighter than 10 Jy. Black boxes around point sources are for purposes of collecting image statistics. (b) Normalized flux density estimates, $\hat{\mathcal{I}}_M^{\text{norm}}$, as a function of distance from image center. Bands indicate an approximate “1 σ ” uncertainty arising from sidelobe confusion and intrinsic randomness of electric fields simulated for point sources in the sky model. Gray and red bands correspond to optimal and erroneous cases respectively, where in the latter, all antennas were erroneously assumed to be identical and of the first type. The dashed and solid line styles correspond to point sources in the westward and south-westward directions respectively. In the optimal case, the normalized estimates are consistent with unity to within “1 σ ” in almost all regions of the image, whereas in the erroneous case, they are mis-estimated (underestimated) with high significance ($\gtrsim 5\sigma$) in most regions of the image. There is no significant difference in estimates between the two different directions of point sources studied.

Table 1. Radio telescopes and array layouts.

| Telescope | Core size b_{max} (in m) | Number of Antennas N_A | Antenna size A_a (in m ²) | Frequency f_0 (in MHz) |
|------------------------|--------------------------------------|-----------------------------|--|-----------------------------|
| MWA-112 ^a | 1400 | 112 | 16 | 150 |
| MWA-240 ^a | 1400 | 240 | 16 | 150 |
| MWA-496 ^a | 1400 | 496 | 16 | 150 |
| MWA-112 ^a | 1400 | 1008 | 16 | 150 |
| LOFAR-LC ^b | 3500 | 24 | 5809 | 50 |
| LOFAR-HC ^b | 3500 | 48 | 745 | 150 |
| LWA1 | 100 | 256 | 10 | 50 |
| LWA-OV ^c | 200 | 256 | 10 | 50 |
| HERA-19 | 70 | 19 | 154 | 150 |
| HERA-37 | 98 | 37 | 154 | 150 |
| HERA-331 | 294 | 331 | 154 | 150 |
| HERA-6769 ^d | 1330 | 6769 | 154 | 150 |
| SKA1-LC ^e | 1000 | 750 | 962 | 150 |
| SKA1-LCD ^f | 1000 | 192,000 | 2 | 150 |
| CHIME | 100 | 1280 | 8 | 600 |
| HIRAX ^g | 200 | 1024 | 28 | 600 |

^a MWA-N denotes N tiles in the specified core diameter

^b LC and HC denotes low band and high band stations inside the specified core diameter

^c Owens Valley LWA

^d Hypothetically chosen to have a total collecting area of 1 km²

^e This is the number of beamformed stations expected to be in the core, roughly three-fourths of the total number

^f All dipoles inside the core are used as independent elements without station beam-forming

^g Hydrogen Intensity mapping and Real-time Analysis eXperiment

ing future trajectory of HERA like systems will be clearly favoured by MOFF imaging. The dotted line is similarly a hypothetical trajectory for the MWA with more tiles added inside the same core diameter. The gray shaded area is for a projected LWA expansion and is also predominantly in the region favouring MOFF imaging. It is bounded by the LWA1 and LWA-OV on the left and right respectively. The current (see Table 1) and a hypothetical expanded layout with a four-fold increase in number of elements over a 50 per cent increase in b_{max} provide the bounds at the bottom and top respectively. Current instruments such as MWA and LOFAR lie in parameter space favouring visibility-based imaging.

We now consider antenna array layouts described by three essential quantities in radio interferometry, namely, maximum baseline length, number of antennas, and the size of each antenna. Fig. 12 shows the boundaries where the ratio of the number of computations required with visibility-based imaging relative to MOFF imaging is unity. The different colored lines correspond to different antenna sizes (cyan - 1 m², blue - 7 m², purple - 16 m², green - 28 m², orange - 150 m², red - 740 m², gray - 5900 m²). Dashed lines of each color denote the boundary to the left of which the MOFF algorithm is favoured for the corresponding antenna size and vice versa for visibility-based imaging.

There is an upper limit set by the maximum number of antennas for each antenna size that can be densely packed inside various baseline lengths but is not shown on this figure

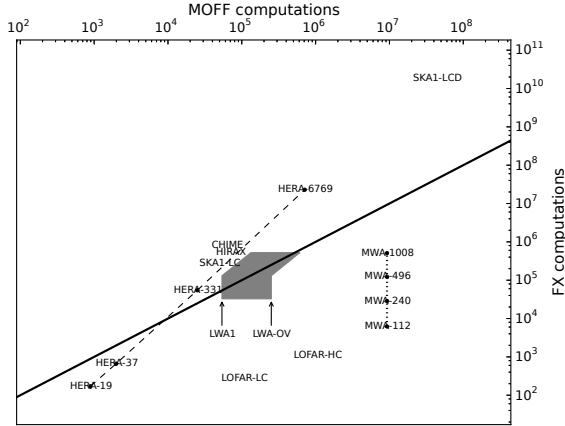


Figure 11. Current and planned instruments in parameter space of number of complex multiplies and adds with MOFF and FX. The solid line is the boundary at which the number of operations with MOFF and visibility-based imaging are equal. MOFF imaging is more efficient for telescopes occupying the left of this line and vice versa. CHIME, HIRAX, SKA1-LC, SKA1-LCD and all the HERA layouts except HERA-19 and HERA-37 lie in the parameter space favoured by MOFF imaging. The dashed line shows the projected trajectory of hypothetical expanded HERA layouts. The dotted line similarly shows hypothetical expanded MWA layouts with more tiles added in the same core. The gray shaded area denotes the projected trajectory of the LWA bounded by LWA1 (left edge), LWA-OV (right edge), current layout (bottom) and a four-fold increase in the number of elements within a 50 per cent increase in the core size (top). Current instruments such as MWA and LOFAR fall in a region favoured by visibility-based imaging.

to avoid crowding. We note that as antenna size increases the maximum number of antennas for a dense packing as a function of baseline length decreases. Hence, this upper limit shifts rightward as antenna size increases. Similarly, with increase in antenna size, N_g also decreases when field of view imaging is achieved with an increased grid spacing equal to antenna size and hence lowers the amount of computations required with the MOFF algorithm. This shifts the dashed lines rightward as well.

The different antennas are color coded by roughly the class of antenna size they fall into. Thus symbols of one color that lie to the left of same colored line indicate MOFF imaging is favoured for those telescopes and vice versa. For e.g., MOFF imaging is favoured in HERA-331 and HERA-6769 because they lie to the left of the orange line but not so in cases of HERA-19 and HERA-37. A majority of the next-generation radio telescopes, namely, HERA-331 and its future expanded versions, SKA1-LC, SKA1-LCD, HIRAX, and CHIME will fall in the regime where MOFF imaging will be desirable. LWA1 and LWA-OV are already very close to the dividing line. Their hypothetical expansions,⁴ will be in the computational regime favoured by MOFF. For a fixed baseline length, regions favouring the MOFF algorithm tend

⁴ LWA1-x2x1 and LWA1-x4x1.5, and LWA-OVx2x1 and LWA-OVx4x1.5 denote two-fold and four-fold increase in number of antennas within a core diameter that is 1 and 1.5 times the current size of 100 m and 200 m respectively for LWA1 and LWA-OV.

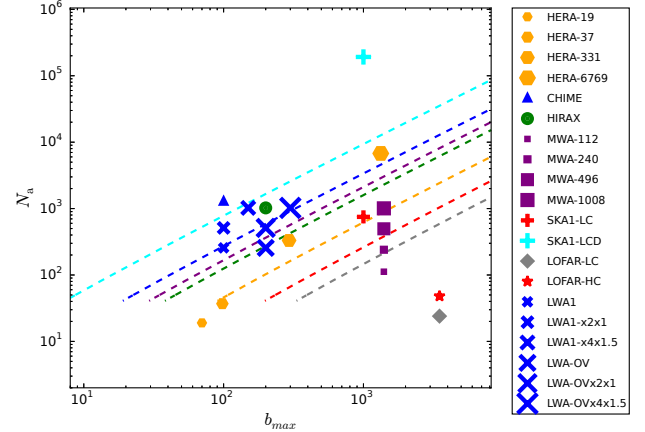


Figure 12. Current and planned instruments in parameter space of baseline length and number of antennas with MOFF and FX. Lines of different colors denote different classes of antenna sizes (cyan - 1 m², blue - 7 m², purple - 16 m², green - 28 m², orange - 150 m², red - 740 m², gray - 5900 m²). Lines of each color denote the boundary to the left of which MOFF algorithm is favoured for the corresponding antenna size. These lines shift rightward with increasing antenna size. The different antennas are color coded by roughly the class of antenna size they fall into. Thus symbols of one color falling to the left of a line of the same color indicate MOFF imaging is advantageous for those telescopes and vice versa. For example, MOFF imaging is favoured in HERA-331 and HERA-6769 because they lie to the left of the orange line but not so in cases of HERA-19 and HERA-37.

to be towards large N_A indicating large-N dense array layouts with smaller antenna elements are best suited for deploying EPIC.

6.2 Data Throughput

We elaborate on the I/O data rates required with the MOFF and visibility-based algorithms. This is particularly relevant in the context of radio transient detection.

Implementation of the MOFF algorithm with EPIC yields calibrated images on time-scales of the output generated by the digitizer and is set by the inverse of the frequency channel width. These calibrated images are accumulated and averaged to a certain time-scale depending on science or hardware requirements, or when the sky has rotated significantly, whichever is lesser. In visibility-based algorithms, the visibilities are accumulated and averaged to this time-scale before images are produced. Thus the data throughput (in samples per second) per cross-polarization with MOFF and X-engine outputs are:

$$r_{\text{MOFF}} \sim \frac{4N_g}{\Delta t} \left(\frac{\Delta B}{\Delta f} \right) \quad (35)$$

$$r_X \sim 2 \frac{N_A(N_A - 1)/2}{\Delta t} \left(\frac{\Delta B}{\Delta f} \right), \quad (36)$$

where, the factor 4 in the expression for r_{MOFF} accounts for imaging after zero-padding the gridded electric fields, the leading factor of 2 in the expression for r_X accounts for the real and imaginary parts of the complex visibilities, ΔB is the bandwidth, Δf is the frequency resolution, and Δt is the

Table 2. Data throughput per cross-polarization for various telescopes with MOFF and X-engine outputs on time-scales of $\Delta t = 10$ ms assuming $\Delta B = 100$ MHz and $\Delta f = 100$ kHz.

| Telescope ^a | r_{MOFF}^b (GB s ⁻¹) ^c | r_X (GB s ⁻¹) ^c |
|------------------------|---|---|
| LWA1 | $\simeq 3$ | $\simeq 24.3$ |
| LWA-OV | $\simeq 12$ | $\simeq 24.3$ |
| HERA-19 | $\lesssim 0.19$ | $\simeq 0.13$ |
| HERA-37 | $\lesssim 0.19$ | $\simeq 0.5$ |
| HERA-331 | $\lesssim 3$ | $\simeq 41$ |
| CHIME | $\lesssim 6.1$ | $\simeq 610$ |

^a Antenna layouts are listed in Table 1.

^b N_g is usually greater than true value because of rounding to the next power of 2 in either direction. Thus r_{MOFF} is usually lesser than the conservative values listed here.

^c We assume 8 bytes for each real sample from MOFF images, and 4 bytes each for real and imaginary parts of visibility samples.

time-scale over which the transient phenomenon is sampled and the data (images or visibilities) are averaged to.

Though a full understanding of the FRB phenomena is yet to emerge, there are indications the time-scales of FRB objects are $\Delta t \sim 1\text{--}10$ ms (Thornton et al. 2013). For a telescope like HERA, $\Delta B \simeq 100$ MHz, $\Delta f \simeq 100$ kHz. For HERA-331, $N_A = 331$ and with a grid spacing to image the field of view, $N_g \simeq 441$ or $N_g \simeq 1024$ if N_g is preferred as a power of 2 in either direction. Using 8 bytes for each floating point sample in the MOFF images and 4 bytes each for real and imaginary parts of visibility samples, the throughputs are $r_{\text{MOFF}} \lesssim 3$ GB s⁻¹ and $r_X \simeq 41$ GB s⁻¹. For HERA-37, $r_{\text{MOFF}} \lesssim 190$ MB s⁻¹ and $r_X \simeq 0.5$ GB s⁻¹. In such a case, The X-engine throughput corresponds to an extreme rate of $\simeq 1.8$ TB an hour per cross-polarization. Conversely, for the same data throughput, the MOFF algorithm can sample even shorter time-scales.

Table 2 shows these data rates for some of the current and planned telescopes for $\Delta t = 10$ ms. In almost all cases listed, even with conservative estimates, the MOFF algorithm provides very economic data throughput for a majority of next generation radio telescopes with a dense layout. The most significant advantage is that calibrated images are also available at no extra cost.

7 CONCLUSIONS

As radio astronomy is entering a new era, advances in instrumentation have to be accompanied by equal advances in processing techniques to manage computational resources. Many future radio telescopes such as the SKA, HERA and LWA are headed towards the large-N dense array layout model for which computational cost from traditional FX/XF correlator-based architecture and visibility-based imaging starts rising steeply. We have provided the first software demonstration of a general purpose imaging algorithm using our generic and efficient EPIC software that is designed to bring this cost down from $\mathcal{O}(N_A^2)$ to $\mathcal{O}(N_g \log_2 N_g)$. Under

the class of direct imaging techniques, ours is one of the most generic – neither does it place any constraint on the array layout to be on a regular grid nor does it require the antenna array to be homogeneous. We have demonstrated its natural ability to robustly image data from heterogeneous arrays and shown that wrong assumptions about array homogeneity result in severe and systematic mis-estimation of the sky model.

Our EPIC package, now publicly available, written in object oriented Python, is highly modularized and parallelizable. It includes an implementation of the MOFF algorithm in addition to visibility-based software holography imaging and a data simulator for sky models. It is designed to provide a development platform to compare different imaging approaches and serve as a stepping stone for real-life GPU/FPGA-based implementation on telescopes. It has been successfully tested on simulated MWA observations as well as real LWA observations from both imaging and calibration view points.

The MOFF algorithm packaged with EPIC is already found to be most suitable for many present and planned radio telescopes such as the LWA, HERA, CHIME, HIRAX and SKA. In general, MOFF is most suited to operate in the region of parameter space characterized by dense packing of a large number of antennas especially when consisting of a large number of small antenna elements.

It is seen to have significant savings in data throughput relative to a X-engine based pipeline. A unique advantage is the instantaneous availability of calibrated time-domain images at no extra cost. Hence, it is a compelling candidate for time-domain radio astronomy, e.g. search for and monitoring of transients. Potentially, it could allow on-chip processing thus lowering even further the already relatively low I/O bandwidth shown in Table 2 except when a transient event is detected. Transient detection pipelines at the backend of EPIC can be fine-tuned to target fast transients such as the Fast Radio Bursts (FRB; Thornton et al. 2013) on millisecond time-scales at GHz frequencies or slow transients from planetary and exoplanetary origins at frequencies around 100 MHz.

Thus, EPIC with the MOFF algorithm packaged is uniquely poised to offer a substantial advantage to imaging with large-N dense arrays typical of next-generation radio telescopes as well as push the frontiers of time-domain astronomy to fill gaps in understanding the science behind phenomena responsible for extreme transient events in the Universe.

In the near future, we plan to demonstrate its speed and precision by upgrading EPIC to a GPU-based implementation in order to operate on real-time data and develop a transient trigger and monitor backend. In the meanwhile, we plan to demonstrate imaging with non-coplanar arrays and direction-dependent calibration.

ACKNOWLEDGEMENTS

We thank Larry D’Addario, Gregg Hallinan, Joseph Lazio and Harish Vedantham for their valuable inputs, and Greg Taylor for providing us with LWA data. This work has been supported by the National Science Foundation through award AST-1206552. Construction of the LWA has been

supported by the Office of Naval Research under Contract N00014-07-C-0147. Support for operations and continuing development of the LWA1 is provided by the National Science Foundation under grant AST-1139974 of the University Radio Observatory program.

REFERENCES

- Bandura K., et al., 2014, in Society of Photo-Optical Instrumentation Engineers (SPIE) Conference Series. p. 22 ([arXiv:1406.2288](#)), doi:10.1117/12.2054950
- Beardsley A. P., et al., 2012, *MNRAS*, **425**, 1781
- Beardsley A. P., Thyagarajan N., Bowman J. D., Morales M. F., 2016, preprint, ([arXiv:1603.02126](#))
- Bhatnagar, S. Cornwell, T. J. Golap, K. Uson, J. M. 2008, *A&A*, **487**, 419
- Bowman J. D., et al., 2013, *Publ. Astron. Soc. Australia*, **30**, 31
- Brigham E. O., 1974, The fast Fourier Transform
- Bunton J. D., 2004, *Experimental Astronomy*, **17**, 251
- Cooley J. W., Tukey J. W., 1965, *Math. Comput.*, **19**, 297
- Cornwell T. J., Golap K., Bhatnagar S., 2008, *IEEE Journal of Selected Topics in Signal Processing*, **2**, 647
- Daishido T., et al., 2000, *Proc. SPIE*, **4015**, 73
- DeBoer D. R., et al., 2016, preprint, ([arXiv:1606.07473](#))
- Ellingson S. W., et al., 2013, *IEEE Transactions on Antennas and Propagation*, **61**, 2540
- Foster G., Hickish J., Magro A., Price D., Zarb Adami K., 2014, *Monthly Notices of the Royal Astronomical Society*, **439**, 3180
- Lonsdale C. J., Doeleman S. S., Cappallo R. J., Hewitt J. N., Whitney A. R., 2000, in Butcher H. R., ed., Society of Photo-Optical Instrumentation Engineers (SPIE) Conference Series Vol. 4015, Radio Telescopes. pp 126–134
- Maneewongvatana S., Mount D. M., 1999, eprint [arXiv:cs/9901013](#),
- Mellema G., et al., 2013, *Experimental Astronomy*, **36**, 235
- Morales M. F., 2011, *PASP*, **123**, 1265
- Morales M. F., Matejek M., 2009, *MNRAS*, **400**, 1814
- Otobe E., et al., 1994, *PASJ*, **46**, 503
- Parsons A. R., et al., 2010, *The Astronomical Journal*, **139**, 1468
- Tegmark M., 1997a, *Phys. Rev. D*, **55**, 5895
- Tegmark M., 1997b, *ApJ*, **480**, L87
- Tegmark M., Zaldarriaga M., 2009, *Phys. Rev. D*, **79**, 083530
- Tegmark M., Zaldarriaga M., 2010, *Phys. Rev. D*, **82**, 103501
- Thompson A. R., Moran J. M., Swenson Jr. G. W., 2001, *Interferometry and Synthesis in Radio Astronomy*, 2nd Edition. Wiley
- Thornton D., et al., 2013, *Science*, **341**, 53
- Thyagarajan N., et al., 2015a, *ApJ*, **804**, 14
- Thyagarajan N., et al., 2015b, *ApJ*, **807**, L28
- Tingay S. J., et al., 2013, *PASA - Publications of the Astronomical Society of Australia*, **30**
- Wijnholds S., van der Veen A.-J., 2009, *Signal Processing, IEEE Transactions on*, **57**, 3512
- Zernike F., 1938, *Physica*, **5**, 785
- Zheng H., et al., 2014, *MNRAS*, **445**, 1084
- de Vos M., Gunst A., Nijboer R., 2009, *Proceedings of the IEEE*, **97**, 1431
- van Cittert P. H., 1934, *Physica*, **1**, 201
- van Haarlem M. P., et al., 2013, *A&A*, **556**, A2

APPENDIX A: SOFTWARE ARCHITECTURE

EPIC is built using object oriented programming in Python and is built on carefully crafted modules which closely rep-

resent real-life entities in radio interferometer arrays and observations. The essential modules along with their key attributes and methods are illustrated in Fig. A1. These modules are described below.

A1 Antenna Module

The antenna module is a fundamental building block upon which all the other modules are built. There is one antenna module per antenna each having attributes – the propagated electric field time-series, $\vec{E}(t)$, and spectrum $E(f)$ for both polarizations. The most important function inside this module is the F-engine that Fourier transforms time-series electric field data into spectra.

The other function (not shown in the figure) is to update the data as new data streams in. This can also be parallelized. Another important attribute consists of antenna flags (not shown in the figure) for each polarization appropriate for the data stream being held by the module.

A2 Interferometer Module

The interferometer module holds the attributes and functions pertaining to a pair of antennas and represents the cross-correlation information obtained from the pair. Its primary attributes are the two antenna modules. It also contains four cross-polarized visibility time-series (even for the FX correlator for diagnostic purposes) and spectra.

The critical component of the interferometer module is the X-engine. This is essentially a software analog of hardware correlators of real telescope systems. The X-engine can be toggled between two states of operation, namely, the FX and XF modes. The FX mode obtains the electric field spectra, $E(f)$ from the individual antenna modules inside this module and multiplies the two to obtain visibility spectra, $V(f)$. On the other hand, the XF mode cross-correlates the electric field time-series from its Antenna modules to obtain the visibilities as a function of lags, $V_t(\tau)$, which is then Fourier transformed to obtain $V(f)$. Both modules can operate on dual-polarizations to obtain all four cross-polarizations.

The other attributes (not shown in the figure) are the flags applicable for each cross-polarization for the current data stream. Similar to the antenna module, it has an update function that can update the visibilities $V_t(\tau)$ or $V(f)$ directly rather than through the electric fields of its component antennas. This functionality is to allow EPIC to operate while attached to the backend of traditional correlator systems. This feature is not utilized for purposes of this paper.

This module forms the fundamental unit for the interferometer array module (to be discussed below) and in general for visibility-based correlator and imaging systems.

A3 Antenna Array Module

The antenna array module consists of all the antenna modules as its attributes and represents the collective properties of its component antennas. By virtue of holding each antenna data independently in their respective modules, the F-engine for the entire array can be distributed to the F-engines of the component antenna modules thus achieving a

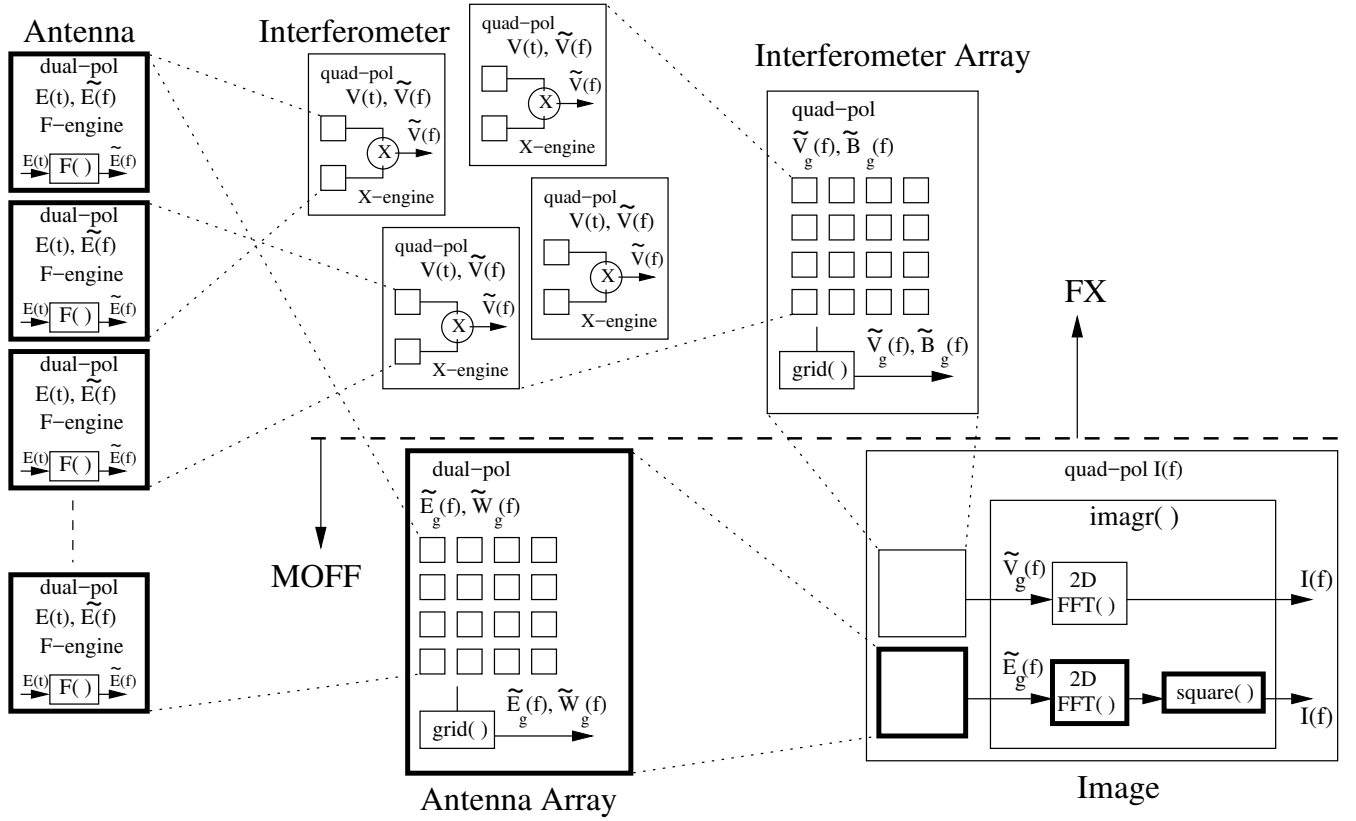


Figure A1. Software architecture of EPIC with core modules, their essential attributes and functions. The antenna module forms the fundamental building block. It consists of electric field time-series and spectra and the F-engine that performs a temporal FFT to obtain electric field spectra from the time-series. The interferometer module is made of a pair of antenna modules. Its main function is the X-engine (FX or XF) to produce visibility spectra. The antenna array module is made of all individual antenna modules as its components and contains collective properties about the antenna subsystems. Its core function is the creation of antenna-to-grid mapping, gridded aperture weights and electric fields. The interferometer array module is very similar in principle to the antenna array module except it operates on cross-correlations and produces gridded visibilities. The image module takes gridded electric fields or visibilities and performs a two-dimensional spatial FFT (and squares the intermediate image in case of the former) to produce output images. Broadly, the MOFF algorithm is implemented by modules below the horizontal dashed line while the visibility-based imaging uses modules above the line. The exact processing pathway implementing the MOFF algorithm is shown in bolded modules.

highly parallelized F-engine while emulating real telescope systems.

The primary attributes held by this module are the antenna aperture illumination weights and electric fields projected on the grid using the gridding convolution method described above and implemented by the gridding function in this module. Significant parts of the antenna-to-grid mapping and gridding convolution are parallelizable across antennas and frequencies.

Individual antenna flags are carried over as additional weights to be applied to the gridded aperture illumination and electric fields. A series of data streams can be stacked up to take advantage of the array optimization available in Python. This module is also equipped to manage dual-polarization.

A4 Interferometer Array Module

Similar to the antenna array module, the interferometer array module consists of individual interferometer modules. It can parallelize the correlator operations by distributing the X-operation over the X-engines of its component inter-

ferometer modules. The interferometer-to-grid mapping and gridding convolution are very similar in nature to that of the antenna array module. Flag-based grid weights, stacking and ability to handle all four cross-polarizations are built into this module.

A5 Image Module

The image module is built as a general purpose module that can switch between operating on gridded electric fields or visibilities. At its heart, it consists of a two-dimensional spatial FFT where the padding can be specified by the user to control the resolution in the output images. In case of MOFF imaging, there is an additional step of squaring the holographic electric field images.

Besides its core functions of spatial Fourier transform and squaring, it can stack, accumulate and average images, and optionally remove the antenna auto-correlations centred around the zero-spacing pixel in the uv plane. It also handles all four cross-polarization products. Currently, it supports writing data out in standard FITS format.

This paper has been typeset from a $\text{\TeX}/\text{\LaTeX}$ file prepared by the author.